





High-angular-momentum Rydberg states in a room-temperature vapor cell for dc electric-field sensing

Alisher Duspayev ^{1,*} Ryan Cardman ^{1,†} David A. Anderson ² and Georg Raithel ¹

¹*Department of Physics, University of Michigan, Ann Arbor, Michigan 48109, USA*

²*Rydberg Technologies Inc., Ann Arbor, Michigan 48103, USA*



(Received 20 October 2023; accepted 27 March 2024; published 7 May 2024)

We prepare and analyze Rydberg states with orbital quantum numbers $\ell \leq 6$ using three-optical-photon electromagnetically induced transparency (EIT) and radio frequency (rf) dressing, and employ the high- ℓ states in electric-field sensing. Rubidium-85 atoms in a room-temperature vapor cell are first promoted into the $25F_{5/2}$ state via Rydberg-EIT with three infrared laser beams. Two rf dressing fields then (near-)resonantly couple the $25F$, $25H$ ($\ell = 5$), and $25I$ ($\ell = 6$) Rydberg states. The dependence of the rf-dressed Rydberg-state level structure on rf powers, rf and laser frequencies is characterized using EIT. Furthermore, we discuss the principles of dc-electric-field sensing using high- ℓ Rydberg states and experimentally demonstrate the method using test electric fields of $\lesssim 50$ V/m induced via photo-illumination of the vapor-cell wall. We measure the highly nonlinear dependence of the dc-electric-field strength on the power of the photo-illumination laser. Numerical calculations, which reproduce our experimental observations well, elucidate the underlying physics. Our paper is relevant to high-precision spectroscopy of high- ℓ Rydberg states, Rydberg-atom-based electric-field sensing, and plasma electric-field diagnostics.

DOI: [10.1103/PhysRevResearch.6.023138](https://doi.org/10.1103/PhysRevResearch.6.023138)

I. INTRODUCTION

Rydberg-atom-based sensors for electromagnetic fields are a prominent example how atomic-physics research is being translated into applications (for recent reviews see, for example [1–4]), offering high sensitivities, large bandwidth, traceability and self-calibration [5,6]. Modern Rydberg field sensors avoid complex apparatuses by the use of room-temperature vapor cells and electromagnetically induced transparency (EIT) [7] for optical interrogation of field-sensitive Rydberg atoms [8], allowing hybridization with existing classical technologies and the realization of portable instrumentation [6,9–11]. Beyond demonstrations of electric field sensing with atomic Rydberg states [5,12,13], Rydberg sensors have proven their potential utility in modulated signal reception from long-wavelength radio frequencies to millimeter-wave [14–16], phase detection [17,18], polarization measurements [9,14,19,20], spatial field mapping, and rf imaging [21–23], and in the establishment of atomic measurement standards [13,24–26].

More recently, two-photon Rydberg-EIT has been generalized to three optical photons [27–29], which afford operation at all-infrared wavelengths [30–33], allow efficient Doppler-shift cancellation conducive to narrower EIT

linewidth [34], and offer inroads towards excitation of high-angular-momentum ($\ell \geq 3$) Rydberg states for electric-field detection in very high and ultrahigh frequency bands [35,36] or even terahertz electrometry [37]. High- ℓ Rydberg states exhibit large sensitivities to dc fields [38] due to their dc electric polarizabilities, which scale as n^7 (with principal quantum number n) and also increase with ℓ [39]. Hence, n and ℓ can be traded in favorable ways to achieve high dc-field sensitivity at a comparatively low n , where optical excitation pathways are more efficient than at high n , and where Rydberg-atom interactions (which typically scale with high powers of n) are less limiting. These aspects are expected to be particularly relevant to field sensing in plasmas [40–44] and ion-beam sources [45,46]. For potential use in the latter [47–49], methods for Rydberg EIT plasma field measurement and diagnostics have been developed [43] and microfield sensing using Rydberg atoms has recently been demonstrated [50].

Motivated by prospects in plasma-field sensing, here we investigate the response of high- ℓ Rydberg atoms to electric fields in a vapor cell. We prepare $25F$, $25G$, $25H$, and $25I$ ($\ell = 3$ to 6) Rydberg states in rubidium-85 (^{85}Rb) using three-optical-photon EIT and up to two radio-frequency (rf) dressing fields. The efficacy of high- ℓ Rydberg-state preparation is verified by measurements of Autler-Townes (AT) splittings induced by the rf dressing fields. dc electric fields are created by photoillumination of the dielectric vapor-cell wall using 453-nm light [51], and the response of the high- ℓ Rydberg states to the dc fields is explored. The paper is organized as follows. In Sec. II, we outline the benefits of high- ℓ Rydberg states for dc-field sensing. In Sec. III, we describe our experimental setup and the utilized rf dressing methods. In Sec. IV, we explain our method of creating dc electric

*alisherd@umich.edu

†Present address: Physical Sciences Inc., Andover, Massachusetts 01810, USA.

Published by the American Physical Society under the terms of the Creative Commons Attribution 4.0 International license. Further distribution of this work must maintain attribution to the author(s) and the published article's title, journal citation, and DOI.

fields by illuminating the cell wall with a 453-nm laser. We then present our dc-field sensing results, which include an approximate calibration of the weak dc field in the vapor cell versus 453-nm illumination power. In the concluding Sec. V, possible applications and research venues for future work are discussed.

II. HIGH- ℓ RYDBERG STATES IN STATIC ELECTRIC FIELDS

Rydberg atoms are very sensitive to external electric fields [39]. Applications discussed in Sec. I include the measurement of electric fields in plasmas and ion sources. In a recent cold-atom study [50], $\ell = 1$ (P) states were employed at relatively high- n to measure electric fields on the order of a few tens of V/m with $\ell = 3$ (F) states to increase sensitivity to weaker electric fields. In this paper, we increase the Rydberg-state electric-field sensitivity by extending to higher ℓ Rydberg states beyond $\ell = 3$, while also using considerably lower n Rydberg states, which exhibit larger optical oscillator strengths, scaling as n^{-3} [26,39], affording stronger spectroscopic signals. Lower- n states also provide the benefit of being less sensitive to Rydberg-atom interactions [52,53], making them suitable for Rydberg-atom applications in inert buffer gases and in low-pressure discharge plasmas. The latter applications benefit from a room-temperature vapor-cell platform [43,51], which we employ in the present paper. Electric polarizabilities increase quickly with ℓ , which is key to reducing n while maintaining a desired level of field sensitivity. Lastly, electric-dipole transition matrix elements between high- ℓ Rydberg states are large ($\sim n^2$) [26,39], allowing efficient rf dressing to access higher- ℓ states with relatively weak rf fields.

In Fig. 1, we have calculated Stark maps of Rb Rydberg states near $n = 25$ for two exemplary values of $|m_J|$, the conserved component of the electronic angular momentum in the direction of the dc electric field, E_{dc} . Throughout paper, for Rydberg-atom dc and ac polarizabilities, as well as for one- and two-photon Rabi frequencies, we employ methods as described, for instance, in Ref. [54], which include a method to compute electric-dipole matrix elements as well as standard time-independent and time-dependent perturbation theory up to second order. Our Fortran codes utilize model potentials from Ref. [55] and published quantum defects of Rb. The Stark spectrum in Fig. 1, as well as all subsequent model spectra are also computed with Fortran codes. In our present paper on $n = 25$ Rydberg states, we employ basis sets ranging from about $n = 10$ to 70 to compute Rydberg-atom properties and spectra. The Stark maps in Fig. 1 visualize the quadratic Stark effect of the levels $|n = 25, \ell, J, m_J\rangle$, indicating a large increase in polarizability from $\ell = 3$ to 7. The quadratic Stark shifts,

$$\Delta W = -\frac{1}{2}\alpha_{dc}|E_{dc}|^2, \quad (1)$$

are given by state-dependent electric polarizabilities, α_{dc} . The latter can be calculated as

$$\alpha_{dc}(m_J) = \alpha_S + \alpha_T \frac{3m_J^2 - J(J+1)}{J(2J-1)}, \quad (2)$$

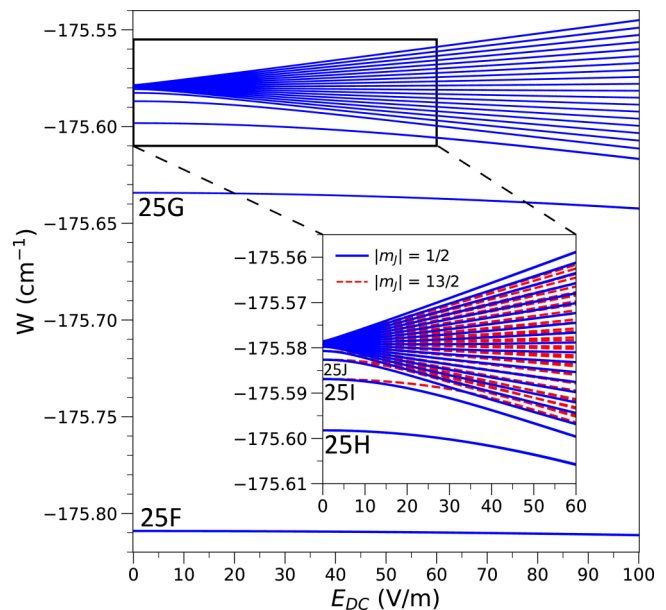


FIG. 1. Computed Stark maps for ^{85}Rb $n = 25$ and two sample cases of $|m_J|$, and zoomed-in detail in the inset, illustrating the increasingly sensitive quadratic response of Rydberg atoms to weak dc electric fields as ℓ increases from $\ell = 3$ ($25F$) to $\ell = 7$ ($25J$). The fine structure is not resolved in this figure

with (n, ℓ, J) -dependent scalar and tensor polarizabilities α_S and α_T , respectively. Table I lists calculated values of α_S , α_T , and α_{dc} for the $n = 25$ high- ℓ Rydberg states utilized in our paper. As one can see, the tensor contributions are substantial. In the experiments discussed in the following sections, only states with $|m_J| = 1/2, 3/2, 5/2$ are coupled and relevant to electric-field sensing. It is apparent that α_{dc} increases by a fac-

TABLE I. Calculated scalar and tensor, and $|m_J|$ -dependent [see Eq. (2)] dc electric polarizabilities, α_S , α_T , and $\alpha_{dc}(|m_J|)$ respectively, [all in MHz/(V/m) 2] for the high- ℓ Rydberg states used in our paper.

State	α_S	α_T	$ m_J $	α_{dc}
$25F_{5/2}$	0.010037	-0.003492	1/2	0.012830
			3/2	0.010735
			5/2	0.006544
$25G_{7/2}$	0.039466	-0.014841	1/2	0.050067
			3/2	0.045827
			5/2	0.037346
$25H_{9/2}$	0.106447	-0.042547	1/2	0.134812
			3/2	0.127720
			5/2	0.113538
			7/2	0.092264
			9/2	0.063899
$25I_{11/2}$	0.247529	-0.105721	1/2	0.314806
			3/2	0.303273
			5/2	0.280206
			7/2	0.245606
			9/2	0.199474
			11/2	0.141808

tor of ≈ 3 with each increment in ℓ . Thus, with our progression from F to I states, Stark shifts increase by about a factor of 30. Here we are able to measure Stark shifts as low as about 3 MHz, corresponding to E_{dc} sensitivity limits of ~ 20 V/m and ~ 4 V/m for $25F$ and $25I$ states, respectively. These sensitivities are suitable for measuring electric fields in plasmas. The approximate $\sim n^{-7/2}$ scaling of the field sensitivity as a function of n may be used to match sensitivity requirements elsewhere.

III. EXCITATION OF $\ell \leq 6$ RYDBERG ATOMS IN A ROOM-TEMPERATURE VAPOR CELL

We use a multiphoton scheme with up to six photons to access high- ℓ states for electric-field sensing in a vapor cell. We first describe the optical three-photon Rydberg-EIT setup, which provides optical spectroscopic access to the Rb $25F_{5/2}$ Rydberg states. Then, we describe the three modes of strong rf drive using additional one-, two-, and three-rf-photon couplings, which we employ to extend the state space to include $25G_{7/2}$, $25H_{9/2}$, and $25I_{11/2}$ states, respectively. These high- ℓ states are then utilized to measure weak dc electric fields.

A. Experimental setup

We concentrate on the ^{85}Rb isotope, but analogous experiments could be performed with other Rb isotopes and atomic species. Three laser beams are aligned colinearly into a room-temperature cell of length $L_c \approx 7.5$ cm filled with a natural Rb vapor, as illustrated in Fig. 2(a). The energy-level diagram in Fig. 2(b) identifies the utilized atomic transitions. The three lasers driving transitions have approximate wavelengths of 795 nm, 762 nm, and 1280 nm, and are referred to as EIT probe, dressing, and coupler lasers, respectively [27,28]. The probe laser is an external-cavity diode laser (ECDL) that is locked to the Doppler-free $5S_{1/2}, F=3 \rightarrow 5P_{1/2}, F=3$ transition on the ^{85}Rb D1 line using saturation spectroscopy. A small portion of the 795-nm light is redshifted by $\Delta_r = -42$ MHz and counteraligned with a small portion of the 762-nm dressing laser, which also is an ECDL, in a separate two-photon EIT reference vapor cell. The 762-nm dressing laser is locked to the $5P_{1/2}, F=3 \rightarrow 5D_{3/2}, F=4$ EIT line in this separate cell, resulting in a shift of $\Delta_d = -\Delta_r \frac{795\text{nm}}{762\text{nm}} = 44$ MHz. In the measurement cell in Fig. 2(a), the 795-nm laser probes the $5S_{1/2}, F=3 \rightarrow 5P_{1/2}, F=3$ resonance for atoms near zero velocity along the z axis, and the 762-nm laser is blue-detuned by $\Delta_d = 44$ MHz from the zero-velocity $5P_{1/2}, F=3 \rightarrow 5D_{3/2}, F=4$ resonance.

The tunable ≈ 1280 -nm coupler laser drives the transition to the $25F_{5/2}$ Rydberg state. While the coupler laser is scanned, the transmission of the locked probe is detected using a photodiode [PD in Fig. 2(a)]. The PD current is amplified in a transimpedance amplifier, and the resultant EIT signal is recorded on an oscilloscope. Each experimental spectrum is an average of typically 300 scans. To calibrate the coupler-laser frequency scan, a portion of the 1280-nm laser power is sent through a Fabry-Pérot (FP) etalon with a free spectral range of 374 MHz whose transmission resonances are recorded simultaneously with the spectroscopic measurements and used as frequency test points in post-processing.

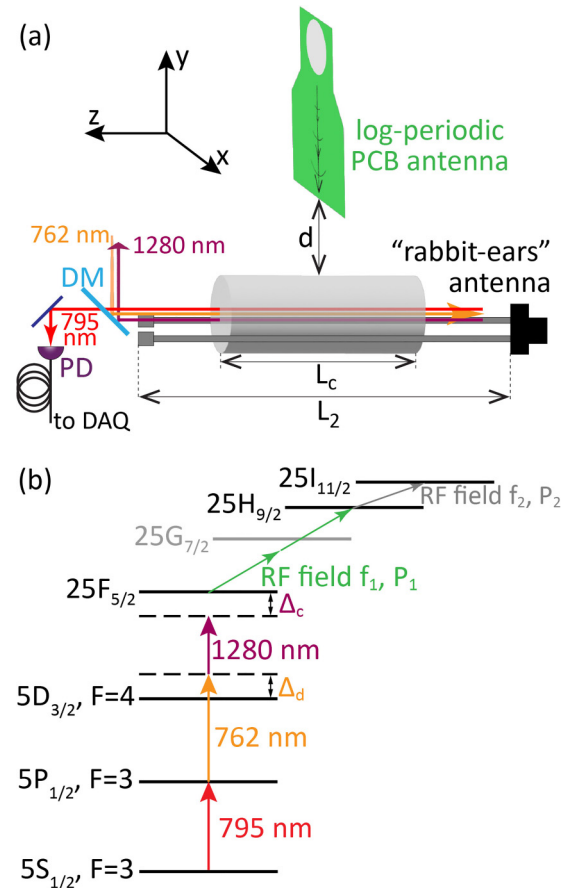


FIG. 2. Sketch of the experimental setup (a) and the energy-level diagram (b) (not to scale). See text for details.

For higher-resolution coupler-laser frequency calibration, we also rf-modulate the beam sample in a fiber electro-optic modulator before passing it through the FP, generating a higher density set of frequency test points.

The probe and the coupler lasers are colinear in the measurement cell [$+z$ direction in Fig. 2(a)], while the dressing beam is counteraligned to them ($-z$ direction). We use various dichroic mirrors [DM in Fig. 2(a), only one is shown] to align the lasers of the different wavelengths through the cell. The counteralignment of the probe and dressing beams helps with preventing leakage of dressing light onto the PD used to record the EIT spectra. Further, by routing the beams through polarization-maintaining fibers, we ensure that all lasers have horizontal polarization [parallel to x in Fig. 2(a)]. The beams are focused into the cell with full width at half maximum (FWHM) of the intensity of ≈ 80 μm for the probe and ≈ 250 μm for the dressing beam and the coupler. Typical powers are ≈ 10 μW , ≈ 8 mW and ≈ 15 mW for the probe, the dressing and the coupler beams, respectively. To raise the three-photon EIT signal, we first find and optimize the two-photon EIT signal on the $5S_{1/2} \rightarrow 5P_{1/2} \rightarrow 5D_{3/2}$ cascade [see Fig. 2(b)] while scanning the dressing beam (with the coupler blocked). With the dressing beam properly aligned and locked, we unblock the coupler and scan it to search for the three-photon EIT signal. Once the three-photon EIT signal

has been located, it is optimized further by fine-tuning the coupler alignment.

To drive rf Rydberg-Rydberg transitions from $25F_{5/2}$, we use two different antennas to access different frequency ranges. The first is a log-periodic planar printed-circuit-board (PCB) antenna with 7 dBi isotropic antenna gain for frequencies between 1 and 10 GHz, which emits an x -polarized field [see Fig. 2(a)]. This rf line starts with a signal generator with power P_1 , followed by a coaxial cable (11 dB loss) connection to a 40-dB-gain amplifier and PCB antenna. The antenna is mounted above the cell at a distance of $d \approx 15$ cm, which is marginally in the antenna far-field, and is oriented to coalign the polarization of the microwave with the laser polarizations in the cell. In this paper, the PCB antenna is used to drive the $25F_{5/2} \leftrightarrow 25G_{7/2}$ and $25F_{5/2} \leftrightarrow 25H_{9/2}$ transitions [field with frequency f_1 in the range 3.14–3.18 GHz for the latter transition and power P_1 in Fig. 2(b)]. A second telescopic rabbit-ears antenna is fed directly by a second signal generator (0.9 dB loss due to another coaxial-cable transmission line) to apply the rf field driving the $25H_{9/2} \leftrightarrow 25I_{11/2}$ transition [field with frequency f_2 in the range 320–360 MHz and power P_2 in Fig. 2(b)]. The rabbit-ears antenna, shown in Fig. 2(a), is folded such that it brackets the vapor cell in the xz -plane with its ears parallel along z to generate linear rf polarization along x , and a small offset in $-y$ to avoid obstructing the alignment of the laser beams. The optimal leg length, which is on the order of $c/(4f_2)$, where c is the speed of light, is kept at $L_2 \approx 22$ cm to maximize the rf field inside the cell.

B. $25F_{5/2} \leftrightarrow 25H_{9/2}$ transition

Experimental scans of f_1 and P_1 for the log-periodic antenna driving the two-photon $25F_{5/2} \leftrightarrow 25H_{9/2}$ transition are shown in Figs. 3(a) and 3(c), respectively (the rabbit-ears antenna is off). In (a), $P_1 = -8$ dBm at the signal generator, corresponding to about 21 dBm injection into the antenna, after taking cable losses and amplifier gain into account. With the 7 dBi isotropic antenna gain, we estimate an rf electric field at the atoms of about 41 V/m. Corresponding calculations of dressed-state energy levels for the optically accessed $m_J = 1/2, 3/2$ and $5/2$ manifolds are shown in Figs. 3(b) and 3(d), with symbol area proportional to the F -state probability in the dressed states, which gives an approximate relative measure for EIT signal strength. In the calculations, we use the absolute intensity unit dBI defined with reference to $I_0 = 1$ W/m², i.e., the intensity $P(\text{dBI}) = 10 \log_{10}[I/(1 \text{ W/m}^2)]$ with intensity I in SI units. The calculations include off-resonant ac shifts of all states in the rf field and utilize computed two-photon matrix elements between $|25F_{5/2}, m_J\rangle$ and $|25H_{9/2}, m_J\rangle$.

In detail, in all presented calculations the quantization axis is parallel to the field polarization (all fields are polarized along x in Fig. 2). The Rydberg state space then breaks up into three sets of two states, $\{|25F_{5/2}, m_J\rangle, |25H_{9/2}, m_J\rangle\}$, which are microwave coupled with an m_J -dependent rf Rabi frequency and exhibit said ac (and, in Sec. IV, dc) shifts. Here, the rf fields are generally too small for high-field Floquet physics [56] to become relevant. Hence, the computational work mostly relies on obtaining the polarizabilities and the Rabi frequencies, with little extra effort to diagonalize small

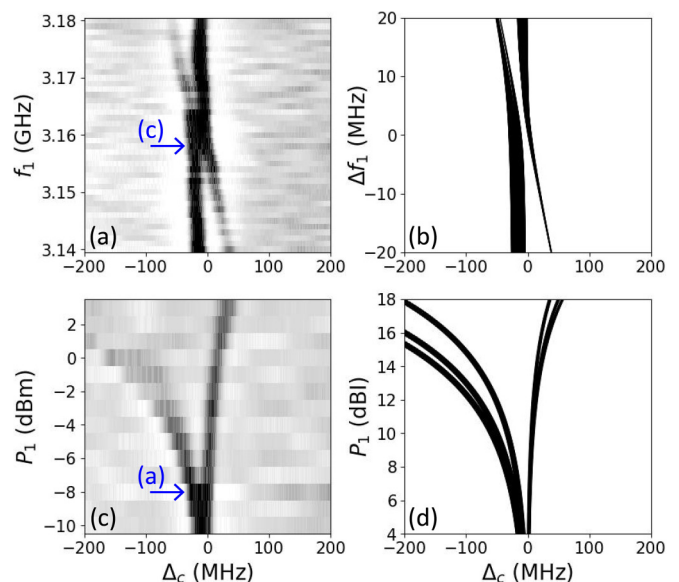


FIG. 3. Spectroscopy of the $25F \leftrightarrow 25H$ two-photon transition vs coupler-laser detuning. Experimental frequency and power scans are shown in (a) and (c), respectively, with the corresponding calculations in (b) and (d). In the experimental data in (a) and (c), the y axes show absolute frequency, f_1 , and power at the signal generator, P_1 , respectively, and the signals are displayed on a linear gray scale. In the theory, plots the areas of the symbols show approximate signal strength. In (b), the y axis shows half of the two-photon detuning from the low-field resonance, and in (d) intensity in dBI (0 dBI = 1 W/m²).

dressed-state matrices and to extract the optically coupled $|25F_{5/2}, m_J\rangle$ amplitudes of the dressed states. In the calculations in Figs. 3(b) and 3(d), there are six bands (one unresolved) that correspond to a total of six dressed states for $|m_J| = 1/2, 3/2$, and $5/2$.

Generally, we obtain very good agreement between the experimental data and the supporting computations, including measured two-photon AT splittings and electric-field signal strengths. There are three AT pairs, one for each optically coupled m_J . From Fig. 3(a), one can conclude that the two-photon resonance occurs at ≈ 3.158 GHz, i.e., the weak-field energy level difference is $h \times 6.316$ GHz, which agrees with the calculated energy-level difference to within 1 MHz. As P_1 is increased, the redshifted AT peak in Fig. 3(c) exhibits larger shifts and broadening than the blueshifted one, and approaches the noise floor at $P_1 \gtrsim 1$ dBm. The strong m_J -splitting of the lower AT branch, visible in Fig. 3(d) at an intensity of $P_1 > 12$ dBI, is marginally resolved in the experimental data in Fig. 3(c). The asymmetry of the pattern in Figs. 3(c) and 3(d) results from the combination of AT splitting and ac shifts. By comparing measured and calculated spectra in Figs. 3(c) and 3(d), one obtains an approximate atomic power calibration of $P_1(\text{dBI}) = P_1(\text{dBm}) + 14.5$ dB. Taking into account the 1 dBm step size in the experimental data in Fig. 3(c), the calibration uncertainty on this is ± 1 dB. Also, the rf electric-field amplitude at $P_1 = -8$ dBm is $E_{\text{rf1}} = 58 \pm 7$ V/m, which is sufficiently precise for the present objective. The measured field exceeds the field estimated from the rf transmission line by about 40%, which

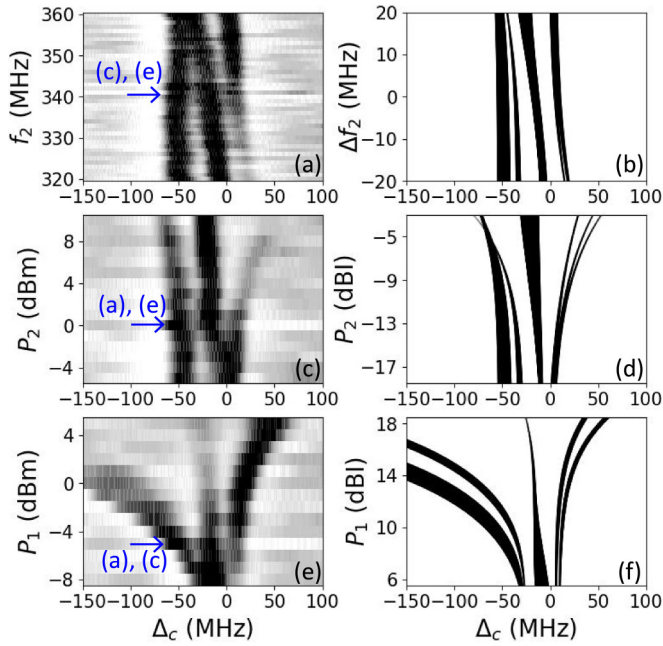


FIG. 4. Spectroscopy of the $25F \leftrightarrow 25H \leftrightarrow 25I$ transition with both rf fields on vs coupler-laser detuning. Experimental frequency and power scans of the signal generator driving the $25H \leftrightarrow 25I$ transition are shown in (a) and (c), respectively. A power scan of the signal generator driving the $25F \leftrightarrow 25H$ transition is shown in (e). The y axes show absolute frequency, f_1 , in (a), and powers at the respective signal generators in (c) and (e), and the signals are displayed on a linear gray scale. Corresponding calculations are presented in (b), (d), and (f). In the theory plots, the areas of the symbols show approximate signal strength. The y axis in (b) shows detuning from the $25H \leftrightarrow 25I$ resonance, and those in (d) and (f) rf field intensities in units dBI.

may be attributable to the facts that the vapor cell is only borderline in the far field, and that the vapor cell is bracketed by the metallic rabbit-ears antenna. While the calibration of the PCB-antenna field suffices for the present purpose, we note an AT line broadening in Fig. 3, which likely is due to rf field inhomogeneity caused by the dielectric glass cell [57,58] and the closely spaced rabbit-ears antenna. From the AT line broadening we infer an rf electric-field inhomogeneity on the order of $\pm 20\%$.

C. $25F_{5/2} \leftrightarrow 25H_{9/2} \leftrightarrow 25I_{11/2}$ transitions

We use the rabbit-ears antenna to drive the $25H_{9/2} \leftrightarrow 25I_{11/2}$ transition. In this case, there are three rf-coupled Rydberg states (per $|m_J\rangle$), leading to the three dressed-state peaks in the experimental spectra in Fig. 4. The $|m_J\rangle$ splittings are partially resolved in the calculations. The calculations include off-resonant ac shifts of all states caused by both rf fields, and we use two-photon matrix elements for the $|25F_{5/2}, m_J\rangle \leftrightarrow |25H_{9/2}, m_J\rangle$ and one-photon matrix elements for the $|25H_{9/2}, m_J\rangle \leftrightarrow |25I_{11/2}, m_J\rangle$ transitions. As before, only the optically accessed $m_J = 1/2, 3/2$ and $5/2$ manifolds are relevant. In detail, the Rydberg state space consists of three sets of three states, $\{|25F_{5/2}, m_J\rangle, |25H_{9/2}, m_J\rangle, |25I_{11/2}, m_J\rangle\}$, which are coupled

by the two fields, with m_J -dependent rf Rabi frequencies, and are ac shifted by both fields. The field frequencies f_1 and f_2 are sufficiently different that a two-field dressed-state description applies. The $|25F_{5/2}, m_J\rangle$ amplitudes in the total of nine optically coupled dressed states, yield the EIT line strengths in Figs. 4(b), 4(d) and 4(f). While several m_J splittings are resolved in the calculations in Figs. 4(b), 4(d) and 4(f), these are not resolved in the present experimental data, leaving three broadened peaks in the measurements in Figs. 4(a), 4(c) and 4(e). Regardless, overall good agreement between the experimental data and the theory is observed.

For the scan of f_2 in Fig. 4(a), it is $P_1 = -5$ dBm and $f_1 = 3.158$ GHz, the resonance frequency found in Fig. 3, and the power into the rabbit-ears antenna is set at $P_2 = 0$ dBm. The $25H_{9/2} \leftrightarrow 25I_{11/2}$ resonance is observed at ≈ 340 MHz, which agrees with our calculated value of 339.6 MHz within uncertainties. The value $f_2 = 340$ MHz is chosen for the P_1 and P_2 scans in Figs. 4(c) and 4(e).

Investigating the power dependence, we observe that as P_2 is increased in Fig. 4(c), while holding P_1 at -5 dBm, the rightmost peak blueshifts and disappears at $P_2 \gtrsim 8$ dBm. In the corresponding calculations in Fig. 4(d), the rightmost peak m_J splits into three lines, while their approximate signal strengths (proportional to symbol area in the theory plots) significantly diminish, in agreement with the experimental data in Fig. 4(c). At the same time, the leftmost and central lines remain relatively strong throughout the tested P_2 -range and experience small redshifts. As P_2 is increased, in experiment [Fig. 4(c)] and calculation [Fig. 4(d)] the oscillator strength redistributes into the central line. Comparing Figs. 4(c) and 4(d), we calibrate P_2 and find $P_2(\text{dBI}) = P_2(\text{dBm}) - 13.5 \text{ dB} \pm 1 \text{ dB}$. The main source of uncertainty is the step size in P_2 of 1 dBm. Again, in the present context, an approximate atomic calibration is sufficient. At a power of $P_2 = 0$ dBm, the electric-field amplitude $E_{\text{rf}2} = 5.8 \pm 0.7$ V/m. For this field, a distance of 3 cm between the legs of the rabbit-ears antenna, and for impedance-matched coupling, the rf power feeding the antenna would be about -10 dBm. Factoring in transmission-line losses and some (likely) impedance mismatch, this is reasonably close to the actual signal generator power of $P_2 = 0$ dBm. From the broadening of the rightmost peak in Fig. 4(c) and the unresolved m_J splitting that underlies the peak, we infer that the rf electric-field inhomogeneity of the 340-MHz field has an upper limit on the order of 20%.

Finally, we explore the effect of varying P_1 on the three-peak EIT spectra in Fig. 4(e). Here $f_2 = 340$ MHz and $P_2 = 0$ dBm. As can be seen in Fig. 4(e), the observed shifts as well as the signal-strength distribution change quite dramatically; this is because the F to H transition is a two-photon transition. First, the rightmost peak exhibits positive shifts, similar to Fig. 4(c). However, opposite to Fig. 4(c), it becomes the strongest peak. This peak would be expected to m_J split [see Fig. 4(f)]. Due to the intrinsic EIT linewidth (FWHM of ≈ 18 MHz) and likely inhomogeneities of the rf intensities within the cell, in the experiment we observe line broadening instead of splitting [see Fig. 4(e)]. Second, the central peak, while slightly redshifting, almost disappears at $P_1 > 3$ dBm, in accordance with the calculations in Fig. 4(f). Finally, we observe that the leftmost line massively redshifts (by ≈ 150 MHz at $P_1 \sim 0$ dBm). Here, the m_J splitting, seen

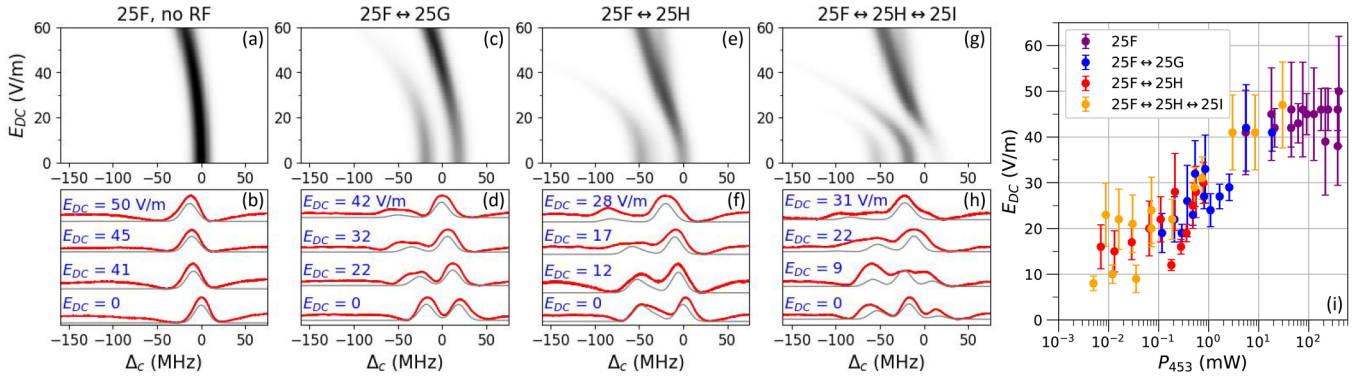


FIG. 5. (a), (c), (e), (g) Calculated EIT spectra vs coupler-laser detuning, Δ_c , and dc electric field, E_{dc} , with the indicated rf transitions applied. Corresponding experimental EIT spectra in selected light-induced dc electric fields are shown in (b), (d), (f), and (h) (bold red curves), together with corresponding spectra at fixed E_{dc} from the plots above that best match the experimental data (gray curves). The calculated spectra (in gray) show calculated EIT line strength, $T(\Delta_c)$, and are slightly offset from the experimental data for clarity. The best-fit E_{dc} values extracted from the match of each measured spectrum to the calculated spectra are indicated. Best-fit E_{dc} values versus 453-nm photoillumination laser power, P_{453} , are shown in (i).

in the calculation in Fig. 4(f), is borderline resolved in the experiment.

IV. DC-FIELD SENSING

In this section, we utilize Rydberg states with $\ell \leq 6$ prepared as described in the previous section for dc-electric-field sensing. The method of creating dc fields by photo-illumination of the vapor-cell wall is first reviewed, followed by experimental measurements of the dc fields. The atomic-calibration-based estimates for E_1 and E_2 are employed to model the experimental data.

A. Creating dc fields in vapor cell by wall photoillumination

Applying dc electric fields to atomic vapors confined in glass cells has turned out to be a considerable challenge [5,8,13], as these devices exhibit a robust isolation against external static fields. Random, weak electric fields (sometimes referred to as microfields) [59–61] may still be present and require an experimental characterization [62]. Charges generating the microfields may arise from effects including photo-ionization of atoms, and collisions involving atoms in Rydberg [39,63] or low-lying intermediate states (such as $5P_{1/2}$ and $5D_{3/2}$) [64,65].

To demonstrate dc electric field measurement using high- ℓ Rydberg states, in the present paper, we require a simple method to generate dc test fields in the cell. While electrodes inside the cell or the cell walls [9,38,66,67] can be used for that, in the present experiments we only had cells without internal electrodes. Therefore, we use an alternative method to generate the test dc fields, in which free charges are generated on the cell walls by laser illumination and photoelectric effect [68]. In Refs. [69,70], this approach was utilized to create patch regions with local electric fields on glass surfaces. It has also been shown that the light-induced dc fields can be quite homogeneous and reach up to ~ 60 V/m within the vapor cell [51].

In our paper, a 453-nm laser beam of ≈ 1 cm diameter that forms a small ($\approx 20^\circ$) angle with respect to the cell axis is

aligned in a way that it illuminates a cell-wall section close to one of the legs of the rabbit-ears antenna along the entire length of the cell. This generates an approximately homogeneous dc electric field, E_{dc} , within the EIT laser beams passing through the cell. The field E_{dc} is approximately parallel to all laser and rf electric fields in our setup, which all point along x in Fig. 2 (a). The dependence of the E_{dc} magnitude on 453-nm laser power is highly nonlinear [51]. Hence, in addition to showing that high- ℓ Rydberg-EIT is suitable for measurement of dc electric fields in vapor cells, in effect we also determine what 453-nm laser power results in what level of E_{dc} in our experiment.

B. Overview of results

In Figs. 5(a), 5(c), 5(e), and 5(g), we plot calculated EIT maps versus coupler-laser detuning and E_{dc} . The calculation for the rf-dressed Rydberg levels is similar to those in Secs. III B and III C, with the addition of the dc Stark shifts using the dc polarizabilities from Table I. This yields rf-dressed Rydberg-level energies, $\Delta W(k, m_J)$, and corresponding $|25F, m_J\rangle$ amplitudes, $c(k, m_J)$, where k is a dressed-state label counting from 1 to up to 3 for each m_J (which is conserved for all-parallel electric fields). Only levels with $|m_J| = 1/2, 3/2$ or $5/2$ are coupled. We then use an empirical finding according to which the EIT line strengths scale with $|\Omega_C \Omega_P|^2$, where Ω_P is the probe Rabi frequency on the transition $|5S_{1/2}, F = 3, m_F\rangle \leftrightarrow |5P_{1/2}, F' = 3, m_{F'} = m_F\rangle$, and Ω_C is the effective two-photon coupler Rabi frequency on the transition $|5P_{1/2}, F' = 3, m_F\rangle \leftrightarrow |25F_{5/2}, F''', m_F\rangle$ transition. Ω_C is coherently summed over all intermediate, detuned states $|5D_{3/2}, F'', m_F\rangle$, where the summing index is F'' . Performing all sums over m_F and the unresolved Rydberg hyperfine structure, F''' , one finds EIT line strengths proportional to $S(k, |m_J|) = |c(k, |m_J|)|^2 w(|m_J|)$, where the Rydberg physics is contained in the determination of the $|25F, |m_J|\rangle$ amplitudes in the rf-dressed states, $c(k, |m_J|)$, and the EIT readout physics in the $|m_J|$ weights, $w(|m_J|)$.

In Figs. 3 and 4, which are focused on multilevel AT splittings and ac shifts in our one- and two-field dressed-state

systems, we show estimated EIT line strength via the areas of the symbols, which are proportional to magnitude squares of the $c(k, |m_J|)$. The weights due the optical EIT-readout physics, $w(|m_J|)$, are, in our case, about $w(|m_J|) = 0.43, 0.29$, and 0.28 for $|m_J| = 1/2, 3/2$, and $5/2$, respectively. While the weak dependence of the $w(|m_J|)$ on the intermediate-state detuning Δ_d in Fig. 2(b) is not significant in our present paper, the variation of the $w(|m_J|)$ values with $|m_J|$ is sufficiently large that in our dc field modeling in Fig. 5 the $w(|m_J|)$ are taken into account. There, EIT is observed when the coupler detuning Δ_c equals to one of the dressed-state energies, $\Delta W(k, |m_J|)$. To obtain the model spectra displayed in the top row in Fig. 5, we convolute the EIT lines with identical Gaussian line profiles, $g(\Delta)$, with FWHM of 18 MHz (the approximate width of the $25F$ EIT line without rf dressing fields), and sum over all $(k, |m_J|)$. The net calculated EIT signal, plotted in Figs. 5(a), 5(c), 5(e), and 5(g), is

$$T(\Delta_c) = \sum_{|m_J|, k} S(k, |m_J|) g[\Delta_c - \Delta W(k, |m_J|)].$$

In the calculations, the dc electric field, E_{dc} , is varied in steps of 1 V/m, equal to about one-tenth of the uncertainty of the measured dc fields.

In Figs. 5(b), 5(d), 5(f), and 5(h), exemplary experimental EIT spectra for the corresponding cases are shown, together with the best-matching spectra from the calculated maps above. For clarity, the calculated spectra are slightly offset from the experimental data. Measured and computed spectra are matched empirically, which is sufficient at the present level. In Fig. 5(i), we plot the matched values of E_{dc} from all other panels of the figure versus 453-nm photo-illumination power, P_{453} . There, we approximately calibrate the dc electric field as a function of illumination power using high- ℓ Rydberg EIT spectroscopy for our experimental setup. The colors of the data points correspond with the transition schemes indicated above Figs. 5(a), 5(c), 5(e), and 5(g), visualizing that accessing higher- ℓ Rydberg states extends the sensitivity range to lower E_{dc} . In the remainder of the paper, we discuss these results in detail.

C. Detailed analysis of results

In Figs. 5(a) and 5(b), it is apparent that the $25F_{5/2}$ -state, which has the lowest polarizabilities among the states tested here, only exhibits significant Stark shifts, exceeding about 10 MHz, for $E_{dc} \gtrsim 40$ V/m, which already is near the largest fields that we can generate with the photoillumination method used. As E_{dc} is increased further to 50 V/m (by increasing P_{453}), the experimental spectra merely shift by an additional 3–5 MHz and exhibit a slight broadening. Increasing n aids in achieving a stronger response of $nF_{5/2}$ states. For example, the $57F_{5/2}$ EIT peak was seen to disappear entirely at our maximum P_{453} (not shown). In the following, we employ rf dressing at $n = 25$ to access higher- ℓ Rydberg states at the same n to elicit a stronger dc electric-field response, afforded by the higher polarizabilities of those states (see Table I).

Increasing ℓ by driving the $25F_{5/2} \leftrightarrow 25G_{7/2}$ transition with the log-periodic antenna ($f_1 = 5.234$ GHz, $P_1 = -20$ dBm), moderately enhances the response, as seen in Figs. 5(c) and 5(d). The two AT peaks start to notably change at $E_{dc} \gtrsim$

20 V/m. The left AT peak shifts and broadens considerably more than the right one. At fields $E_{dc} \gtrsim 40$ V/m, the left AT peak diminishes greatly in signal strength and eventually becomes indiscernible while becoming more responsive to changes in E_{dc} . This behavior reflects the fact that the dressed state associated with the left AT peak turns into the stronger-shifting $25G_{7/2}$ state, which has a larger polarizability than the $25F_{5/2}$ state. As the $25G_{7/2}$ character of the lower AT peak increases, its EIT signal strength diminishes due to the diminishing optical coupling to the $5D_{3/2}$ state [see Fig. 2(b)]. Conversely, with increasing E_{dc} , the right AT peak acquires an increasing amount of $25F_{5/2}$ character, which reduces its response to changes in E_{dc} while its EIT signal strength increases.

Increasing ℓ further by driving the $25F_{5/2} \leftrightarrow 25H_{9/2}$ two-photon microwave transition (see Sec. III B) allows for further E_{dc} -response enhancement, as seen in Figs. 5(e) and 5(f). Here f_1 and P_1 for the log-periodic antenna are 3.158 GHz and -5 dBm, respectively. Already at $E_{dc} \gtrsim 10$ V/m, the two AT peaks significantly change. The left AT peak in Figs. 5(e) and 5(f) shifts and broadens considerably more than in Figs. 5(c) and 5(d), and at $E_{dc} \gtrsim 30$ V/m its strength drops to hardly noticeable. These features reflect the even larger polarizability of the $25H_{9/2}$ state, which lowers the detectable E_{dc} . The excess broadening [Fig. 5(e)] and splitting [Fig. 5(f)] of the $25F_{5/2}$ -like upper AT peak at fields $E_{dc} \gtrsim 30$ V/m results from an increase of the m_J splitting caused by the ac Stark effect of the $25F_{5/2}$ state in the rather strong two-photon rf drive field, $E_{rf1} \approx 80$ V/m.

Finally, we utilize both the PCB and rabbit-ears antennas to assess the response of the three-peak EIT on the $25F_{5/2} \leftrightarrow 25H_{9/2} \leftrightarrow 25I_{11/2}$ ladder to the dc fields in Fig. 5(h). Here, f_1 and P_1 are same as in Fig. 5(f), while $f_2 = 345$ MHz and $P_2 = 4$ dBm. In this most E_{dc} -field-sensitive case, we have utilized finer steps in P_{453} (and, hence, in E_{dc}) to resolve the spectral changes in fields $E_{dc} \lesssim 10$ V/m. First, the rightmost peak appears to redshift and merge into the central peak, and the signal strength redistributes between the peaks. At $E_{dc} \gtrsim 20$ V/m, first the most redshifting line acquires increasing $25I_{11/2}$ -character and greatly diminishes in signal strength, followed by an increasingly $25H_{9/2}$ -like state departing to the redshifted side. At larger fields, the $25F_{5/2}$ -like peak dominates and eventually becomes the only visible peak left, and the spectrum looks similar to Figs. 5(e) and 5(f).

In all four cases in Fig. 5, the theoretical predictions qualitatively agree with the experimental data. Figure 5 demonstrates the stepwise increase in dc electric-field sensitivity with increasing ℓ , probed via three-photon optical Rydberg EIT. The discrepancies between measurements and calculations are attributed to imperfections in the optical and rf polarizations, inhomogeneities in both the rf and dc fields, and environmental magnetic fields, which were not shielded. Especially at small E_{dc} , the latter may cause m_J mixing and Zeeman shifts of the high- ℓ states on the order of ± 5 MHz. In view of Table I, the m_J mixing may alter the spectra due to the large tensor polarizabilities.

At $E_{dc} \sim 0$ and for rf parameters that lead to efficient mixing of the coupled levels, the polarizabilities of the mixed levels are approximately given by the averages over the polarizabilities of the coupled states. In Fig. 5, these averages

are to be taken over the levels printed over the tops of the four data sets. Assuming that the $|m_J|$ range is restricted to $|m_J| \leq 5/2$, i.e., the states that are optically coupled for all x -polarized fields, the averages are 0.010, 0.027, 0.068, and 0.145 MHz/(V/m)² for Figs. 5(a), 5(c), 5(e), and 5(g), respectively. At small E_{dc} , all dressed levels in a given plot should Stark shift with roughly equal curvatures, and the curvature ratios between the four sets of plots in Figs. 5(a), 5(c), 5(e), and 5(g) should roughly accord with the stated numbers. This simplified analysis explains the trends that are observed in Fig. 5 for $E_{dc} \lesssim 15$ V/m, i.e., in regions where the rf coupling amplitudes exceed the Stark shifts for all four cases.

In Fig. 5(i), we plot the E_{dc} values obtained by matching observed and calculated spectra from Figs. 5(a)–5(h) versus the 453-nm photoillumination power, P_{453} , used to generate the dc field. In our analysis, for a given experimental spectrum we first determine the locations of the dominant spectral peaks and then find the calculated spectrum that matches the dominant peaks best. The E_{dc} spacing of the calculations is 1 V/m, which is fine enough for the empirical matching, and is about one-tenth of the typical uncertainty reflected in Fig. 5(i). The selection for the best-matching calculated spectrum is then widened by using the peak FWHM and the relative heights of the peaks as additional matching criteria. The procedure yields an E_{dc} -range over which the variation of the corresponding set of calculated spectra is too small to allow for a finer match between the experimental spectrum with a smaller set of calculated spectra. The center values of said E_{dc} ranges yield the data points in Fig. 5(i), while the full widths of the ranges give the full uncertainty ranges. The resultant uncertainties on the E_{dc} values are below 20% of the respective E_{dc} values. At higher fields, the absolute field uncertainties are larger, pointing to electric-field inhomogeneity being a main cause of uncertainty. In future studies, the matching procedure may be improved by some automation, which would be warranted after addressing the main experimental broadening effects (see Sec. V).

Empirically, in Fig. 5(i) we first observe that for $P_{453} \lesssim 10$ mW the field increases approximately linearly in $\log_{10}(P_{453})$ and saturates at higher powers at values near 50 V/m, in general agreement with earlier findings [51]. In particular, the lowest measured E_{dc} is $\approx 8 \pm 2$ V/m at $P_{453} \approx 5$ μ W, obtained with the most sensitive scheme in which two rf fields are employed to couple the $25F$, $25H$, and $25I$ Rydberg states. The largest measured E_{dc} is $\approx 50 \pm 8$ V/m at $P_{453} \approx 400$ mW, obtained by all-optical Rydberg-EIT to measure the Stark shift of $25F$ without using additional rf fields. The observed highly nonlinear behavior reflects a complex charging or discharging equilibrium within the vapor cell. This topic is beyond the scope of our present paper and may be explored further in future studies. Further, focusing on the label coloring in Fig. 5(i), it is confirmed that with increasing ℓ the range of measurable dc electric fields shifts to lower values. Measurements of the $25F$ state are the least sensitive, on a relative scale, and are helpful to calibrate fields $E_{dc} \gtrsim 45$ V/m, as also seen in Fig. 5(b) and the corresponding calculation in Fig. 5(a). Adding high- ℓ character to the Rydberg states via rf dressing allows us to measure E_{dc} down to ≈ 8 V/m, as also seen in Figs. 5(c)–5(h).

We conclude this section with two comparisons that exemplify the enormous increase of electric polarizability with ℓ . In previous work [51], in which a two-photon Rydberg-EIT probe of Rb $60D_J$ states was used, dc electric fields were measured with a sensing limit of ≈ 25 V/m, i.e., about a factor of ≈ 3 less sensitive than in our present paper. This comparison reflects the fact that polarizability of Rb Rydberg levels increases by about a factor of ≈ 2500 between nD and nI states of the same n , while the polarizability at fixed ℓ scales “only” as $\approx n^7$. In another study with dc electric fields applied via electrodes integrated into the vapor-cell wall [38], a two-photon Rydberg-EIT probe of Rb $32S_{1/2}$ was employed to measure dc fields in the range of 500 V/m.

V. DISCUSSION AND OUTLOOK

We have prepared Rydberg states with $\ell \leq 6$ in a room-temperature vapor cell using a combination of three-photon optical EIT and up to three-photon rf dressing. The rf dressing fields were calibrated by Rydberg-EIT spectroscopy. The resultant well-characterized dressed Rydberg states were then used to measure and calibrate dc electric fields generated by photoelectric effect on the cell walls. The utility of the increased electric polarizabilities of the high- ℓ Rydberg states in measuring weak electric fields was demonstrated. The underlying physics was modeled by accounting for all ac and dc shifts and resonant couplings of the dressed Rydberg-atom system, as well as the specifics of the utilized three-optical-photon Rydberg-EIT probe.

We believe that the main drivers for our ~ 18 MHz EIT linewidth and for the discrepancies seen in Fig. 5 are the stray magnetic field and the field inhomogeneity inherent to dc electric fields induced by photo-illumination. Possible improvements in the setup to extend the electric field sensitivity could include stray-magnetic-field shielding and a reduction of the EIT-laser linewidths. Further improvement may result from a reduction of rf field inhomogeneities and unwanted polarization variations [16,71–73]. Also, in future work focused on exploring the dc-field sensitivity limit of our method, one may reduce the inhomogeneity of E_{dc} by using custom-made vapor cells with internal electrodes connected to the cell exterior via electric feed-throughs (which is technically possible but rather costly and can be subject to long lead times). Solving the Lindblad equation for our case of collinear three-optical-photon Rydberg EIT in a Rb vapor cell, we find that EIT linewidths < 5 MHz should be possible. At the low n -value used in our paper, optical electric-dipole transition matrix elements are relatively large (scaling $\sim n^{-3/2}$) and rf-transition ones relatively small (scaling $\sim n^2$). These scalings favor economical setups, as laser power is more expensive than rf power at sub-5-GHz frequencies. We therefore anticipate applications in high-precision measurements on relatively low- n and high- ℓ Rydberg states [74–76] in room-temperature vapor cells for tests of *ab initio* atomic-physics calculations [26,55,77,78], the exploration of pathways towards excitation of circular Rydberg atoms [79–82], and other applications in fundamental-physics research [83].

Along the lines of applications mentioned in the Introduction, the demonstrated methods could be of interest for sensing electric fields in low-pressure discharge plasmas [84–86].

Combining Rydberg-EIT in low-pressure buffer-gas vapor cells, which was recently observed [87], with plasma generators, one may anticipate future plasma-physics research in discharge plasmas with Rydberg-EIT as an electric-field probe. This may include dusty plasmas [88], which are not only relevant to applications [89,90] but also in astrophysics [91], nonlinear dynamics [92] and condensed matter [93]. Rydberg-EIT as a noninvasive electric-field probe with high spatial resolution [43] employing high- ℓ states could become useful in future dusty-plasma research. On the modeling side, one may introduce m_J couplings caused by spontaneous decay on the EIT ladder and by weak transverse magnetic fields. For ^{85}Rb and the level scheme used in the present paper, this would extend the dimension of the underlying Hilbert space to at least 268. Such large spaces will benefit from a different method to solve the Lindblad equation, such

as the quantum trajectory method that we have introduced in Refs. [94,95] as a powerful tool to treat Rydberg-EIT in large Hilbert spaces.

ACKNOWLEDGMENTS

We would like to thank B. Dash, N. Thaicharoen, M. Viray, and J. MacLennan for useful discussions. This work was supported by the U.S. Department of Energy, Office of Science, Office of Fusion Energy Sciences under Award No. DE-SC0023090, NSF Grant No. PHY-2110049, and Rydberg Technologies, Inc.. A.D. and R.C. acknowledge support from the respective Rackham Predoctoral Fellowships at the University of Michigan.

D.A.A. and G.R. have an interest in Rydberg Technologies, Inc.

-
- [1] C. S. Adams, J. D. Pritchard, and J. P. Shaffer, Rydberg atom quantum technologies, *J. Phys. B* **53**, 012002 (2019).
- [2] D. A. Anderson, R. E. Sapiro, and G. Raithel, Rydberg atoms for radio-frequency communications and sensing: Atomic receivers for pulsed RF field and phase detection, *IEEE Trans. Aerosp. Electron. Syst.* **35**, 48 (2020).
- [3] C. T. Fancher, D. R. Scherer, M. C. St. John, and B. L. S. Marlow, Rydberg atom electric field sensors for communications and sensing, *IEEE Trans. Quantum Eng.* **2**, 1 (2021).
- [4] A. Artusio-Glimpse, M. T. Simons, N. Prajapati, and C. L. Holloway, Modern rf measurements with hot atoms: A technology review of Rydberg atom-based radio frequency field sensors, *IEEE Microwave Magazine* **23**, 44 (2022).
- [5] C. L. Holloway, J. A. Gordon, S. Jefferts, A. Schwarzkopf, D. A. Anderson, S. A. Miller, N. Thaicharoen, and G. Raithel, Broadband Rydberg atom-based electric-field probe for SI-traceable, self-calibrated measurements, *IEEE Trans. Antennas Propag.* **62**, 6169 (2014).
- [6] D. A. Anderson, R. E. Sapiro, and G. Raithel, A self-calibrated SI-traceable Rydberg atom-based radio frequency electric field probe and measurement instrument, *IEEE Trans. Antennas Propag.* **69**, 5931 (2021).
- [7] K.-J. Boller, A. Imamoğlu, and S. E. Harris, Observation of electromagnetically induced transparency, *Phys. Rev. Lett.* **66**, 2593 (1991).
- [8] A. K. Mohapatra, T. R. Jackson, and C. S. Adams, Coherent optical detection of highly excited Rydberg states using electromagnetically induced transparency, *Phys. Rev. Lett.* **98**, 113003 (2007).
- [9] D. A. Anderson, E. G. Paradis, and G. Raithel, A vapor-cell atomic sensor for radio-frequency field detection using a polarization-selective field enhancement resonator, *Appl. Phys. Lett.* **113**, 073501 (2018).
- [10] D. H. Meyer, P. D. Kunz, and K. C. Cox, Waveguide-coupled Rydberg spectrum analyzer from 0 to 20 GHz, *Phys. Rev. Appl.* **15**, 014053 (2021).
- [11] R. Mao, Y. Lin, K. Yang, Q. An, and Y. Fu, A high-efficiency fiber-coupled Rydberg-atom integrated probe and its imaging applications, *IEEE Antennas Wirel. Propag.* **22**, 352 (2023).
- [12] A. Osterwalder and F. Merkt, Using high Rydberg states as electric field sensors, *Phys. Rev. Lett.* **82**, 1831 (1999).
- [13] J. A. Sedlacek, A. Schwettmann, H. Kübler, R. Löw, T. Pfau, and J. P. Shaffer, Microwave electrometry with Rydberg atoms in a vapour cell using bright atomic resonances, *Nat. Phys.* **8**, 819 (2012).
- [14] D. A. Anderson, R. E. Sapiro, and G. Raithel, An atomic receiver for AM and FM radio communication, *IEEE Trans. Antennas Propag.* **69**, 2455 (2021).
- [15] C. Holloway, M. Simons, A. H. Haddab, J. A. Gordon, D. A. Anderson, G. Raithel, and S. Voran, A multiple-band Rydberg atom-based receiver: AM/FM stereo reception, *IEEE Antennas Propag. Mag.* **63**, 63 (2021).
- [16] R. Legaie, G. Raithel, and D. A. Anderson, A millimeter-wave atomic receiver, *AVS Quantum Sci.* **6**, 024402 (2024).
- [17] S. Berweger, A. B. Artusio-Glimpse, A. P. Rotunno, N. Prajapati, J. D. Christesen, K. R. Moore, M. T. Simons, and C. L. Holloway, Closed-loop quantum interferometry for phase-resolved Rydberg-atom field sensing, *Phys. Rev. Appl.* **20**, 054009 (2023).
- [18] P. Vouras, K. Vijay Mishra, and A. Artusio-Glimpse, Phase retrieval for Rydberg quantum arrays, in *ICASSP 2023: 2023 IEEE International Conference on Acoustics, Speech and Signal Processing (ICASSP)* (IEEE, New York City, USA, 2023), pp. 1–5.
- [19] Y. Jiao, L. Hao, X. Han, S. Bai, G. Raithel, J. Zhao, and S. Jia, Atom-based radio-frequency field calibration and polarization measurement using cesium nD_J Floquet states, *Phys. Rev. Appl.* **8**, 014028 (2017).
- [20] Y. Wang, F. Jia, J. Hao, Y. Cui, F. Zhou, X. Liu, J. Mei, Y. Yu, Y. Liu, J. Zhang, F. Xie, and Z. Zhong, Precise measurement of microwave polarization using a Rydberg atom-based mixer, *Opt. Express* **31**, 10449 (2023).
- [21] C. L. Holloway, J. A. Gordon, A. Schwarzkopf, D. A. Anderson, S. A. Miller, N. Thaicharoen, and G. Raithel, Sub-wavelength imaging and field mapping via electromagnetically induced transparency and Autler-Townes splitting in Rydberg atoms, *Appl. Phys. Lett.* **104**, 244102 (2014).
- [22] L. A. Downes, A. R. MacKellar, D. J. Whiting, C. Bourgenot, C. S. Adams, and K. J. Weatherill, Full-field terahertz imaging

- at kilohertz frame rates using atomic vapor, *Phys. Rev. X* **10**, 011027 (2020).
- [23] R. Cardman, L. F. Gonçalves, R. E. Sapiro, G. Raithel, and D. A. Anderson, Atomic 2D electric field imaging of a Yagi-Uda antenna near-field using a portable Rydberg-atom probe and measurement instrument, *Adv. Opt. Technol.* **9**, 305 (2020).
- [24] J. A. Sedlacek, A. Schwettmann, H. Kübler, and J. P. Shaffer, Atom-based vector microwave electrometry using rubidium Rydberg atoms in a vapor cell, *Phys. Rev. Lett.* **111**, 063001 (2013).
- [25] C. L. Holloway, N. Prajapati, J. A. Sherman, A. Rüfenacht, A. B. Artusio-Glimpse, M. T. Simons, A. K. Robinson, D. S. La Mantia, and E. B. Norrgard, Electromagnetically induced transparency based Rydberg-atom sensor for traceable voltage measurements, *AVS Quantum Sci.* **4**, 034401 (2022).
- [26] A. Duspayev and G. Raithel, Gauge effects in bound-bound Rydberg transition matrix elements, *Phys. Rev. A* **105**, 012825 (2022).
- [27] C. Carr, M. Tanasittikosol, A. Sargsyan, D. Sarkisyan, C. S. Adams, and K. J. Weatherill, Three-photon electromagnetically induced transparency using Rydberg states, *Opt. Lett.* **37**, 3858 (2012).
- [28] N. Thaicharoen, K. R. Moore, D. A. Anderson, R. C. Powel, E. Peterson, and G. Raithel, Electromagnetically induced transparency, absorption, and microwave-field sensing in a Rb vapor cell with a three-color all-infrared laser system, *Phys. Rev. A* **100**, 063427 (2019).
- [29] N. Prajapati, N. Bhusal, A. P. Rotunno, S. Berweger, M. T. Simons, A. B. Artusio-Glimpse, Y. Ju Wang, E. Bottomley, H. Fan, and C. L. Holloway, Sensitivity comparison of two-photon vs three-photon Rydberg electrometry, *J. Appl. Phys.* **134**, 023101 (2023).
- [30] P. Thoumany, Th. Germann, T. Hänsch, G. Stania, L. Urbonas, and Th. Becker, Spectroscopy of rubidium Rydberg states with three diode lasers, *J. Mod. Opt.* **56**, 2055 (2009).
- [31] D. P. Fahey and M. W. Noel, Excitation of Rydberg states in rubidium with near infrared diode lasers, *Opt. Express* **19**, 17002 (2011).
- [32] L. A. M. Johnson, H. O. Majeed, and B. T. H. Varcoe, A three-step laser stabilization scheme for excitation to Rydberg levels in 85Rb, *Appl. Phys. B* **106**, 257 (2012).
- [33] S. H. You, M. H. Cai, S. S. Zhang, Z. S. Xu, and H. P. Liu, Microwave-field sensing via electromagnetically induced absorption of Rb irradiated by three-color infrared lasers, *Opt. Express* **30**, 16619 (2022).
- [34] S. M. Bohachuk, F. Ripka, V. Venu, F. Christaller, C. Liu, M. Schmidt, H. Kübler, and J. P. Shaffer, Three-photon Rydberg-atom-based radio-frequency sensing scheme with narrow linewidth, *Phys. Rev. Appl.* **20**, L061004 (2023).
- [35] R. C. Brown, B. Kayim, M. A. Viray, A. R. Perry, B. C. Sawyer, and R. Wyllie, Very-high- and ultrahigh-frequency electric-field detection using high angular momentum Rydberg states, *Phys. Rev. A* **107**, 052605 (2023).
- [36] N. Prajapati, J. W. Kunzler, A. B. Artusio-Glimpse, A. P. Rotunno, S. Berweger, M. T. Simons, C. L. Holloway, Ch. M. Gardner, M. S. Mcbeth, and R. A. Younts, High angular momentum coupling for enhanced Rydberg-atom sensing in the very-high frequency band, *J. Appl. Phys.* **135**, 074402 (2024).
- [37] S. Chen, D. J. Reed, A. R. MacKellar, L. A. Downes, N. F. A. Almuhawish, M. J. Jamieson, C. S. Adams, and K. J. Weatherill, Terahertz electrometry via infrared spectroscopy of atomic vapor, *Optica* **9**, 485 (2022).
- [38] L. Ma, M. A. Viray, D. A. Anderson, and G. Raithel, Measurement of dc and ac electric fields inside an atomic vapor cell with wall-integrated electrodes, *Phys. Rev. Appl.* **18**, 024001 (2022).
- [39] T. F. Gallagher, *Rydberg Atoms* (Cambridge University Press, Cambridge, England, 2005).
- [40] S. Alexiou, A. Weingarten, Y. Maron, M. Sarfaty, and Ya. E. Krasik, Novel spectroscopic method for analysis of nonthermal electric fields in plasmas, *Phys. Rev. Lett.* **75**, 3126 (1995).
- [41] D. Feldbaum, N. V. Morrow, S. K. Dutta, and G. Raithel, Coulomb expansion of laser-excited ion plasmas, *Phys. Rev. Lett.* **89**, 173004 (2002).
- [42] H. Park, R. Ali, and T. F. Gallagher, Probing the fields in an ultracold plasma by microwave spectroscopy, *Phys. Rev. A* **82**, 023421 (2010).
- [43] D. A. Anderson, G. Raithel, M. Simons, and C. L. Holloway, Quantum-optical spectroscopy for plasma electric field measurements and diagnostics, [arXiv:1712.08717](https://arxiv.org/abs/1712.08717).
- [44] B. M. Goldberg, T. Hoder, and R. Brandenburg, Electric field determination in transient plasmas: in situ & non-invasive methods, *PSST* **31**, 073001 (2022).
- [45] N. Bassim, K. Scott, and L. A. Giannuzzi, Recent advances in focused ion beam technology and applications, *MRS Bull.* **39**, 317 (2014).
- [46] J. Gierak, P. Mazarov, L. Bruchhaus, R. Jede, and L. Bischoff, Review article: Review of electrohydrodynamical ion sources and their applications to focused ion beam technology, *J. Vac. Sci. Technol. B* **36**, 06J101 (2018).
- [47] B. Knuffman, A. V. Steele, and J. J. McClelland, Cold atomic beam ion source for focused ion beam applications, *J. Appl. Phys.* **114**, 044303 (2013).
- [48] B. J. Claessens, M. P. Reijnders, G. Taban, O. J. Luiten, and E. J. D. Vredenburg, Cold electron and ion beams generated from trapped atoms, *Phys. Plasmas* **14**, 093101 (2007).
- [49] A. J. McCulloch, B. M. Sparkes, and R. E. Scholten, Cold electron sources using laser-cooled atoms, *J. Phys. B* **49**, 164004 (2016).
- [50] A. Duspayev and G. Raithel, Electric field analysis in a cold-ion source using stark spectroscopy of Rydberg atoms, *Phys. Rev. Appl.* **19**, 044051 (2023).
- [51] L. Ma, E. Paradis, and G. Raithel, dc electric fields in electrode-free glass vapor cell by photoillumination, *Opt. Express* **28**, 3676 (2020).
- [52] X. Han, S. Bai, Y. Jiao, G. Raithel, J. Zhao, and S. Jia, Adiabatic potentials of cesium (nD_j)₂ Rydberg-Rydberg macrodimers, *J. Phys. B* **52**, 135102 (2019).
- [53] A. Gaj, A. Krupp, J. Balewski, R. Loew, S. Hofferberth, and T. Pfau, From molecular spectra to a density shift in dense Rydberg gases, *Nat. Commun.* **5**, 4546 (2014).
- [54] A. Reinhard, T. C. Liebisch, B. Knuffman, and G. Raithel, Level shifts of rubidium Rydberg states due to binary interactions, *Phys. Rev. A* **75**, 032712 (2007).
- [55] M. Marinescu, H. R. Sadeghpour, and A. Dalgarno, Dispersion coefficients for alkali-metal dimers, *Phys. Rev. A* **49**, 982 (1994).
- [56] D. A. Anderson, S. A. Miller, G. Raithel, J. A. Gordon, M. L. Butler, and C. L. Holloway, Optical measurements of strong microwave fields with Rydberg atoms in a vapor cell, *Phys. Rev. Appl.* **5**, 034003 (2016).

- [57] A. P. Rotunno, C. L. Holloway, N. Prajapati, S. Berweger, A. B. Artusio-Glimpse, R. Brown, M. Simons, A. K. Robinson, B. N. Kayim, M. A. Viray, J. F. Jones, B. C. Sawyer, R. Wyllie, T. Walker, R. W. Ziolkowski, S. R. Jefferts, S. Geibel, J. Wheeler, and E. Imhof, Investigating electromagnetically induced transparency spectral lineshape distortion due to non-uniform fields in Rydberg-atom electrometry, *J. Appl. Phys.* **134**, 084401 (2023).
- [58] H. Fan, S. Kumar, J. Sheng, J. P. Shaffer, C. L. Holloway, and J. A. Gordon, Effect of vapor-cell geometry on Rydberg-atom-based measurements of radio-frequency electric fields, *Phys. Rev. Appl.* **4**, 044015 (2015).
- [59] C. F. Hooper, Electric microfield distributions in plasmas, *Phys. Rev.* **149**, 77 (1966).
- [60] A. Y. Potekhin, G. Chabrier, and D. Gilles, Electric microfield distributions in electron-ion plasmas, *Phys. Rev. E* **65**, 036412 (2002).
- [61] A. V. Demura, Physical models of plasma microfield, *Int. J. Spectrosc.* **2010**, 671073 (2010).
- [62] C. L. Holloway, M. T. Simons, J. A. Gordon, A. Dienstfrey, D. A. Anderson, and G. Raithel, Electric field metrology for SI traceability: Systematic measurement uncertainties in electromagnetically induced transparency in atomic vapor, *J. Appl. Phys.* **121**, 233106 (2017).
- [63] I. I. Beterov, D. B. Tretyakov, I. I. Ryabtsev, V. M. Entin, A. Ekers, and N. N. Bezuglov, Ionization of Rydberg atoms by blackbody radiation, *New J. Phys.* **11**, 013052 (2009).
- [64] M. Cheret, L. Barbier, W. Lindinger, and R. Deloche, Penning and associative ionisation of highly excited rubidium atoms, *J. Phys. B* **15**, 3463 (1982).
- [65] L. Barbier, A. Pesnelle, and M. Cheret, Theoretical interpretation of Penning and associative ionisation in collisions between two excited rubidium atoms, *J. Phys. B* **20**, 1249 (1987).
- [66] D. Barredo, H. Kübler, R. Daschner, R. Löw, and T. Pfau, Electrical readout for coherent phenomena involving Rydberg atoms in thermal vapor cells, *Phys. Rev. Lett.* **110**, 123002 (2013).
- [67] J. Grimm, M. Mack, F. Karlewski, F. Jessen, M. Reinschmidt, N. Sándor, and J. Fortágh, Measurement and numerical calculation of rubidium Rydberg Stark spectra, *New J. Phys.* **17**, 053005 (2015).
- [68] D. L. Rousseau, G. E. Leroi, and W. E. Falconer, Charged-particle emission upon ruby laser irradiation of transparent dielectric materials, *J. Appl. Phys.* **39**, 3328 (1968).
- [69] A. M. Hankin, Y.-Y. Jau, L. P. Parazzoli, C. W. Chou, D. J. Armstrong, A. J. Landahl, and G. W. Biedermann, Two-atom Rydberg blockade using direct $6S$ to nP excitation, *Phys. Rev. A* **89**, 033416 (2014).
- [70] Y.-Y. Jau and C. Tony, Vapor-cell-based atomic electrometry for detection frequencies below 1 kHz, *Phys. Rev. Appl.* **13**, 054034 (2020).
- [71] M. Jing, Y. Hu, J. Ma, H. Zhang, L. Zhang, L. Xiao, and S. Jia, Atomic superheterodyne receiver based on microwave-dressed Rydberg spectroscopy, *Nat. Phys.* **16**, 911 (2020).
- [72] C. L. Holloway, N. Prajapati, A. B. Artusio-Glimpse, S. Berweger, M. T. Simons, Y. Kasahara, A. Alú, and R. W. Ziolkowski, Rydberg atom-based field sensing enhancement using a split-ring resonator, *Appl. Phys. Lett.* **120**, 204001 (2022).
- [73] K. Dixon, K. Nickerson, D. W. Booth, and J. P. Shaffer, Rydberg-atom-based electrometry using a self-heterodyne frequency-comb readout and preparation scheme, *Phys. Rev. Appl.* **19**, 034078 (2023).
- [74] J. Lee, J. Nunkaew, and T. F. Gallagher, Microwave spectroscopy of the cold rubidium $(n+1)d_{5/2} \rightarrow ng$ and nh transitions, *Phys. Rev. A* **94**, 022505 (2016).
- [75] S. J. Berl, C. A. Sackett, T. F. Gallagher, and J. Nunkaew, Core polarizability of rubidium using spectroscopy of the ng to nh , ni Rydberg transitions, *Phys. Rev. A* **102**, 062818 (2020).
- [76] K. Moore, A. Duspayev, R. Cardman, and G. Raithel, Measurement of the Rb g -series quantum defect using two-photon microwave spectroscopy, *Phys. Rev. A* **102**, 062817 (2020).
- [77] M. S. Safronova, C. J. Williams, and C. W. Clark, Relativistic many-body calculations of electric-dipole matrix elements, lifetimes, and polarizabilities in rubidium, *Phys. Rev. A* **69**, 022509 (2004).
- [78] M. S. Safronova and U. I. Safronova, Critically evaluated theoretical energies, lifetimes, hyperfine constants, and multipole polarizabilities in ^{87}Rb , *Phys. Rev. A* **83**, 052508 (2011).
- [79] D. A. Anderson, A. Schwarzkopf, R. E. Sapiro, and G. Raithel, Production and trapping of cold circular Rydberg atoms, *Phys. Rev. A* **88**, 031401(R) (2013).
- [80] V. Zhelyazkova and S. D. Hogan, Preparation of circular Rydberg states in helium using the crossed-fields method, *Phys. Rev. A* **94**, 023415 (2016).
- [81] A. Larrouy, S. Patsch, R. Richaud, J.-M. Raimond, M. Brune, C. P. Koch, and S. Gleyzes, Fast navigation in a large Hilbert space using quantum optimal control, *Phys. Rev. X* **10**, 021058 (2020).
- [82] R. Cardman and G. Raithel, Circularizing Rydberg atoms with time-dependent optical traps, *Phys. Rev. A* **101**, 013434 (2020).
- [83] M. S. Safronova, D. Budker, D. DeMille, Derek F. Jackson Kimball, A. Derevianko, and C. W. Clark, Search for new physics with atoms and molecules, *Rev. Mod. Phys.* **90**, 025008 (2018).
- [84] J. E. Harry, *Introduction to Plasma Technology: Science, Engineering, and Applications* (John Wiley & Sons, Weinheim, Germany, 2013).
- [85] J. G. Eden, S.-J. Park, J. H. Cho, M. H. Kim, T. J. Houlahan, B. Li, E. S. Kim, T. L. Kim, S. K. Lee, K. S. Kim, J. K. Yoon, S. H. Sung, P. Sun, C. M. Herring, and C. J. Wagner, Plasma science and technology in the limit of the small: Microcavity plasmas and emerging applications, *IEEE Trans. Plasma Sci.* **41**, 661 (2013).
- [86] S. Nijdam, K. V. Desai, S.-J. Park, P. P. Sun, O. Sakai, G. Lister, and J. Gary Eden, Foundations of plasma photonics: Lamps, lasers, and electromagnetic devices, *PSST* **31**, 123001 (2023).
- [87] N. Thaicharoen, R. Cardman, and G. Raithel, Rydberg-EIT of ^{85}Rb vapor in a cell with Ne buffer gas, [arXiv:2308.07554](https://arxiv.org/abs/2308.07554).
- [88] P. K. Shukla and B. Eliasson, Colloquium: Fundamentals of dust-plasma interactions, *Rev. Mod. Phys.* **81**, 25 (2009).
- [89] L. Boufendi, M. C. Jouanny, E. Kovacevic, J. Berndt, and M. Mikikian, Dusty plasma for nanotechnology, *J. Phys. D* **44**, 174035 (2011).
- [90] S. Ratynskaia, A. Bortolon, and S. I. Krasheninnikov, Dust and powder in fusion plasmas: recent developments in theory, modeling, and experiments, *Rev. Mod. Plasma Phys.* **6**, 20 (2022).
- [91] D. A. Mendis and M. Rosenberg, Cosmic dusty plasma, *Annu. Rev. Astron. Astrophys.* **32**, 419 (1994).

- [92] G. E. Morfill and A. V. Ivlev, Complex plasmas: An interdisciplinary research field, *Rev. Mod. Phys.* **81**, 1353 (2009).
- [93] H. Thomas, G. E. Morfill, V. Demmel, J. Goree, B. Feuerbacher, and D. Möhlmann, Plasma crystal: Coulomb crystallization in a dusty plasma, *Phys. Rev. Lett.* **73**, 652 (1994).
- [94] L. Zhang, S. Bao, H. Zhang, G. Raithel, J. Zhao, L. Xiao, and S. Jia, Interplay between optical pumping and Rydberg EIT in magnetic fields, *Opt. Express* **26**, 29931 (2018).
- [95] Y. Xue, L. Hao, Y. Jiao, X. Han, S. Bai, J. Zhao, and G. Raithel, Rydberg electromagnetically induced transparency in a large Hilbert space, *Phys. Rev. A* **99**, 053426 (2019).